Assessment of the Madden-Julian Oscillation in CMIP6 Models based on Moisture Mode Theory

Qiao-Jun Lin[1], Víctor C. Mayta[1], and Ángel F. Adames Corraliza[1]

[1]Department of Atmospheric and Oceanic Sciences, University of Wisconsin, Madison, Wisconsin, USA

Key Points:

- MJO simulation skill in 25 CMIP6 models is assessed using moisture mode theory.
- No model can realistically reproduce all the moisture mode properties of the MJO over the Indian Ocean.
- Models that best capture the MJO's moisture mode features exhibit more realistic mean states and MJO structure.

Corresponding author: Qiao-Jun Lin, `qiaojun.lin@wisc.edu`

Abstract

The moist processes of the Madden-Julian Oscillation (MJO) in the Coupled Model Intercomparison Project Phase 6 models are assessed using moisture mode theory-based diagnostics over the Indian Ocean (10°S-10°N, 75°E-100°E). Results show that no model can capture all the moisture mode properties relative to the reanalysis. Most models satisfy weak temperature gradient balance but have unrealistically fast MJO propagation and a lower moisture-precipitation correlation. Models that satisfy the most moisture mode criteria reliably simulate the background moist static energy (MSE) and low-level zonal winds compared to models that satisfy the least amount of criteria. The MSE budget associated with the MJO is also well-represented in the good models rather than in the poor models. Our results show that capturing the MJO's moisture mode properties over the Indian Ocean is associated with a more realistic representation of the MJO simulation and thus can be employed to diagnose MJO performance.

Plain Language Summary

The Madden-Julian Oscillation is the most important tropical phenomenon that drives weather at the intraseasonal time scale. Although the MJO has been analyzed for the past decades, its simulation in climate models can still be improved. Previous studies have emphasized that the MJO evolution is tightly modulated by moisture fluctuations and posited the moisture mode theory to explain its behavior. Here, we show that no climate model can realistically reproduce the moist thermodynamics of the MJO, particularly its sensitivity to humidity anomalies. A few models can simulate some basic MJO features.

1 Introduction

The Madden-Julian Oscillation (MJO; Madden & Julian, 1971, 1972) is a planetary-scale envelope of convection that is coupled with the circulation and moisture (Raymond & Fuchs, 2009; Sobel & Maloney, 2013; Á. F. Adames & Kim, 2016, among others). This convective envelope often initiates over the Indian Ocean (IO) and propagates eastward at about 3 to 5 m s^{-1} (C. Zhang & Ling, 2017; Rushley et al., 2022). The MJO affects weather and climate phenomena around the globe through its teleconnections, including Asia and Australian rainfall events (Chang et al., 2021; Bagtasa, 2020; Cowan et al., 2022; Dao et al., 2023), tropical cyclone genesis (J.-M. Chen et al., 2018; Rahul et al., 2022), El Niño Southern Oscillation and Atlantic Niño (Hendon et al., 2007; S.-K. Lee et al., 2023), as well as heatwaves and the frequency of tornadoes and hailstorms in the Northern America (Y.-Y. Lee & Grotjahn, 2019; Miller et al., 2022). In part due to these impacts, many studies in the last decades have tried to better understand the MJO through a combination of observation, theory, and modeling experiments (e.g., Raymond & Fuchs, 2009; Maloney et al., 2010; Sobel & Maloney, 2012; Á. F. Adames & Kim, 2016; Wang et al., 2016, and references therein).

Numerous studies have observed that the growth of MJO convection is associated with feedbacks that increase moisture anomalies (Sobel et al., 2014; Del Genio & Chen, 2015; B. Zhang et al., 2019). Moreover, the eastward propagation of MJO is predominantly governed by horizontal and vertical moisture advection (Kiranmayi & Maloney, 2011; Kim, Kug, & Sobel, 2014; K.-C. Tseng et al., 2015; Á. F. Adames & Wallace, 2015; Hung & Sui, 2018). These features have led to a view of MJO that has become a basis of moisture mode theory. Moisture mode theory posits that the MJO is tightly modulated and organized by moisture fluctuations, while temperature anomalies play a minor role because of weak temperature gradient (WTG) balance (Emanuel et al., 1994; Raymond & Fuchs, 2009; Sobel et al., 2014; Á. F. Adames & Kim, 2016; Á. F. Adames, 2017; Ahmed et al., 2021; A. F. Adames & Maloney, 2021; Mayta & Adames Corraliza, 2023, among others). The processes that lead to the moisture fluctuations also lead to the evolution of moisture mode. According to these conditions, Mayta et al. (2022) proposed a series of moisture mode criteria to analyze the different tropical waves. Further, by using these criteria, Mayta and Adames Corraliza (2023) found that MJO behaves as a moisture mode only over the IO region. Outside this region, temperature fluctuations are as influential as moisture anomalies in MJO's thermodynamics because a faster propagation of MJO prevents WTG balance.

Although our understanding of the MJO has significantly improved, accurate representation of MJO variability remains a major challenge in global climate models (GCMs; Kim et al., 2009; Ahn et al., 2017, 2020). It is well-documented that the failure of models to simulate the MJO is largely a result of inadequate treatment of deep cumulus convection, particularly its insufficient sensitivity to free tropospheric water vapor (e.g., Maloney & Hartmann, 2001; M.-I. Lee et al., 2003; Holloway et al., 2013; Kim, Lee, et al., 2014). Models in which convection is sensitive to water vapor fluctuations produce regions of precipitation that persist at the intraseasonal timescale, hence producing MJO activity. From this, models that have a strong coupling of precipitation with low-level wind field and moisture can simulate more realistic MJO convection (Holloway et al., 2013; Ahn et al., 2017). Furthermore, a strong horizontal gradient of mean state moisture can drive robust MJO propagation (Jiang, 2017; Ahn et al., 2020). All of these features are consistent with the MJO being at least partially explained as a moisture mode.

Based on these previous results, we hypothesize that the moisture mode properties of the MJO are essential for its realistic simulation. To this end, we seek to examine the MJO simulation in the Coupled Model Intercomparison Project Phase 6 (CMIP6) models based on the moisture mode framework (Ahmed et al., 2021; Mayta et al., 2022; Mayta & Adames, 2023). Specifically, we seek to answer the following questions:

- Q1: Can the global climate models reproduce the MJO moisture mode properties over the Indian Ocean?
- Q2: If a model can capture the moisture mode behaviors, does it mean that the model has better skills in the MJO simulation than others?

The structure of this research is as follows. Section 2 describes the datasets and methods. Section 3 diagnoses MJO simulation by the moisture mode theory. In section 4, we compare the good and poor simulations in the moisture mode behaviors against the observations. Major findings are summarized in section 5.

2 Data Description, Processing, and Diagnostics

2.1 Data Sources

25 CMIP6 models (Eyring et al., 2016) are adopted to evaluate MJO simulation in the 20-year (1995-2014) historical scenario (Table 1). We primarily use r1i1p1f1 ensemble member for most models, except for EC-Earth3 (r3i1p1f1), HadGEM3-GC31-LL (r1i1p1f3), HadGEM3-GC31-MM (r3i1p1f3), and UKESM1-0-LL (r1i1p1f2) based on their available data. Models that cannot provide all radiative fluxes to compute net radiation within the atmosphere are marked with asterisks (*).

Observation and reanalysis data are used as a reference for model simulations. We use the moisture, precipitation, temperature, horizontal winds, vertical velocity, geopotential height, radiation, and surface fluxes from the fifth generation of the European Centre for Medium-Range Weather Forecasts (ECMWF) reanalysis (ERA5; Hersbach et al., 2019). The outgoing longwave radiation (OLR) from NOAA Physical Sciences Laboratory (Liebmann & Smith, 1996) is used to calculate the MJO index. The precipitation from Tropical Rainfall Measuring Mission (TRMM; Kummerow et al., 2000) product is applied to compute the realistic wave responses by the space-time power spectra. All data

Models	**Institutions**	**Lat ×Lon**
ACCESS-CM2*	Commonwealth Scientific and Industrial Research Organisation, Australian Research Council Centre of Excellence for Climate System Science	144 × 192
AWI-ESM-1-1-LR	Alfred Wegener Institute, Helmholtz Centre for Polar and Marine Research	96 × 192
BCC-ESM1*	Beijing Climate Center	64 × 128
CESM2	National Center for Atmospheric Research, Climate and Global Dynamics Laboratory	192 × 288
CESM2-FV2		96 × 144
CESM2-WACCM		192 × 288
CESM2-WACCM-FV2		96 × 144
EC-Earth3*	Rossby Center, Swedish Meteorological and Hydrological Institute	256 × 512
FGOALS-g3*	Chinese Academy of Sciences	80 × 180
GFDL-CM4	National Oceanic and Atmospheric Administration, Geophysical Fluid Dynamics Laboratory	90 × 144
HadGEM3-GC31-LL	Met Office Hadley Centre	144 × 192
HadGEM3-GC31-MM		324 × 432
IITM-ESM*	Centre for Climate Change Research, Indian Institute of Tropical Meteorology Pune	94 × 192
INM-CM4-8*	Institute for Numerical Mathematics, Russian Academy of Science	120 × 180
INM-CM5-0*		120 × 180
IPSL-CM6A-LR	Institut Pierre Simon Laplace	143 × 144
IPSL-CM6A-LR-INCA		143 × 144
KACE-1-0-G*	National Institute of Meteorological Sciences/Korea Meteorological Administration	144 × 192
MIROC6*	Japan Agency for Marine-Earth Science and Technology Atmosphere and Ocean Research Institute National Institute for Environmental Studies / RIKEN Center for Computational Science	128 × 256
MPI-ESM-1-2-HAM	Max Planck Institute for Meteorology	96 × 192
MPI-ESM1-2-HR		192 × 384
MPI-ESM1-2-LR		96 × 192
MRI-ESM2-0	Meteorological Research Institute	160 × 320
TaiESM1*	Research Center for Environmental Changes, Academia Sinica	192 × 288
UKESM1-0-LL	Met Office Hadley Centre	144 × 192

Table 1. List of 25 CMIP6 models used in this study, including their research centers and horizontal resolutions. The models with an asterisk (*) mean lack complete radiation fluxes for calculating net radiation heating within the atmosphere.

are interpolated into a uniform horizontal resolution of 2.5° longitude × 2.5° latitude. We discuss the MJO activity during the extended boreal winter (November to April) when the MJO is more active (Q. Zhang et al., 2019; X. Li et al., 2020).

2.2 Filtering, EOF Analysis, and Regressions

The dominant mode of the MJO convection is derived through the empirical orthogonal function (EOF) analysis of 20-96-days bandpass filtered OLR over the equatorial belt (15°S-15°N). The first EOF mode (EOF1) has the largest amplitude around 90°E, corresponding to the MJO convection (not shown). The field variables are regressed onto the first principal component (PC1) time series to obtain a composite of the MJO evolution from -30 to 30 days, following the same process as previous studies (e.g., Á. F. Adames et al., 2021; Mayta et al., 2021; Mayta & Adames Corraliza, 2023). These perturbations are then scaled to one standard deviation of PC1. To make the strongest MJO convection occur near 90°E at lag 0 day in all data, we refer to the basis function approach (J. Lee et al., 2019; Orbe et al., 2020, among others) to project simulated OLR anomalies onto the observed EOF1 and hence obtain the PC1 time series of each model.

2.3 Diagnostic Criteria

In order to evaluate the moist thermodynamics of simulated MJO, we apply the moisture mode criteria over the Indian Ocean (IO; 10°S-10°N, 75E°-100°E) region, where the MJO shows characteristics of a moisture mode (Mayta & Adames Corraliza, 2023). The criteria are (Ahmed et al., 2021; Mayta et al., 2022):

1. *Wave must exhibit a large moisture signature that is highly correlated with the precipitation anomalies*

To be considered a moisture mode, the MJO's precipitation anomalies P' should be sensitive to the column water vapor $\langle q \rangle'$ variations. In other words, it must exhibit a high coherence between $\langle q \rangle'$ and P' ($R_{P,q}$) as follows,

$$\langle q \rangle' \propto P' \tag{1}$$

where $\langle \cdot \rangle \equiv \frac{1}{g}\int_{100}^{1000}(\cdot)dp$ is vertical integration from 1000 to 100 hPa, and primes ($'$) represent the regressed anomalies. The correlation should be higher than 0.9, indicating that the moisture fluctuations significantly modulate the precipitation evolution, at least 81% of the variance. The slope of $\langle q \rangle'$ to P' is the convective moisture adjustment time scale ($\tau_c \equiv \frac{\langle q \rangle'}{P'}$), defined as the time to remove column moisture through the rainfall (Betts, 1986). The τ_c of MJO convection should be about 1 day over the IO region (Mayta & Adames Corraliza, 2023).

2. *The system must be in the weak temperature gradient (WTG) balance*
   Under WTG approximation, the vertical advection of dry static energy $\langle \omega \partial_p s \rangle'$ must exhibit a balance with apparent heat source $\langle Q_1 \rangle'$, expressed as:

$$\langle \omega \partial_p s \rangle' \simeq \langle Q_1 \rangle' \tag{2}$$

   where $s = C_pT + gz$ is dry static energy (DSE). To satisfy this second criterion, the slope of $\langle Q_1 \rangle'$ to $\langle \omega \partial_p s \rangle'$ should be close to 1 in linear least-squares fitting, and their correlation must also be higher than 0.9.
3. *Moisture must govern the evolution of moist static energy*
   If the MJO is a moisture mode, the column water vapor must be the main contributor to its moist static energy (MSE, m), giving the following relation,

$$\langle m \rangle' = \langle s \rangle' + \langle L_v q \rangle' \approx \langle L_v q \rangle' \tag{3}$$

   To guarantee the approximation in Eq. (3), a slope of $\langle L_v q \rangle'$ to $\langle m \rangle'$ must be $\sim$ 1 in linear least-squares fitting ($S_{q,m}$), with a high coherence between both variables (> 0.9).
4. N_{mode}
   The dimensionless N_{mode} parameter is also adopted to quantify the relative importance of column water vapor versus temperature in the evolution of MSE (Á. F. Adames et al., 2019). N_{mode} can be defined as in Á. F. Adames et al. (2019) and Mayta et al. (2022) as follows,

$$\mathrm{N}_{mode} \simeq \frac{c_p^2 \tau}{c^2 \tau_c} \tag{4}$$

   where $c = 50$ m s^{-1} is the phase speed of a first baroclinic free gravity wave, c_p is the phase speed of MJO over the warm pool Indian Ocean, and τ is the characteristic temporal scale of MJO (i.e., $\sim$37 days in the ERA5). The c_p is estimated by using the Radon Transform method (Radon, 1917; Mayta et al., 2023), which is described in the Supplementary Information (SI). The MJO can be classified as a moisture mode when $\mathrm{N}_{mode} \ll 1$ (i.e., $log_{10}\mathrm{N}_{mode} < -0.5$).

3 Moist Thermodynamic Diagnostics of MJO Simulation

As in Mayta et al. (2022), the moisture mode criteria are applied to the reanalysis and models by constructing scatterplots. The results are summarized in Figure 1.

Reanalysis, as recently documented in Mayta and Adames Corraliza (2023), shows a high correlation between $\langle q \rangle'$ and P' over the IO region ($R_{P,q} = 0.95$), whereas the climate models depict an average value of 0.88±0.05. Among them, HadGEM3-GC31-LL, KACE-1-0-G, and TaiESM1 models have the highest correlation ($R_{P,q} = 0.94$). The remaining 15 models underestimate $R_{P,q}$ (< 0.9; black values). The τ_c of ERA5 is about

	$R_{P,q}$	τ_c	$S_{q,m}$	$log_{10}N_{mode}$	
ERA5	0.95	1.02	0.98	-0.69	
ACCESS-CM2	0.88	1.10	0.96	-0.06	
AWI-ESM-1-1-LR	0.92	0.86	0.86	-0.97	×
BCC-ESM1	0.86	0.83	0.89	-0.64	
CESM2	0.85	1.15	0.87	-0.60	
CESM2-FV2	0.92	1.11	0.89	-0.61	○
CESM2-WACCM	0.86	1.05	0.92	-0.57	
CESM2-WACCM-FV2	0.88	1.15	0.89	-0.39	
EC-Earth3	0.89	1.28	1.00	-0.65	○
FGOALS-g3	0.87	1.08	0.87	-0.69	
GFDL-CM4	0.90	0.93	0.90	-0.45	○
HadGEM3-GC31-LL	0.94	1.19	0.97	-0.25	
HadGEM3-GC31-MM	0.92	1.15	0.94	-0.05	
IITM-ESM	0.93	0.99	0.82	-0.98	
INM-CM4-8	0.76	1.08	1.02	-0.02	×
INM-CM5-0	0.80	0.95	1.01	0.00	
IPSL-CM6A-LR	0.84	1.10	0.95	-0.68	
IPSL-CM6A-LR-INCA	0.79	0.98	0.88	-1.03	×
KACE-1-0-G	0.94	1.27	0.95	0.28	
MIROC6	0.88	1.20	0.92	-0.75	○
MPI-ESM-1-2-HAM	0.88	0.60	0.83	-0.94	×
MPI-ESM1-2-HR	0.91	0.83	0.87	-0.94	
MPI-ESM1-2-LR	0.88	0.68	0.85	-0.94	
MRI-ESM2-0	0.88	1.30	1.00	-0.20	
TaiESM1	0.94	1.37	1.05	-0.49	
UKESM1-0-LL	0.92	1.27	0.94	-0.27	

Figure 1. The values of criteria $R_{P,q}$, τ_c, $S_{q,m}$, and $log_{10}\mathrm{N}_{mode}$ from the ERA5 and 25 CMIP6 models. Numbers in blue represent values that satisfy the moisture mode criteria: (1) $R_{P,q}$ > 0.9, and τ_c within ± 0.5 standard deviations relative to the ERA5 (0.93-1.12 days); (2) $S_{q,m}$ $\sim$ 1 (0.9-1.05); and (3) $log_{10}\mathrm{N}_{mode}$ ranges from -0.8 to -0.5. For model selection, the green boxes indicate model values within ± 1.5 standard deviations from the reanalysis, while the orange boxes represent the $log_{10}\mathrm{N}_{mode}$ within the range of -0.8 to -0.3. The relatively good and poor models are marked by the green circles and red crosses, respectively.

1.02 day. Only 10 models are within ± 0.5 standard deviation (SD) relative to the reanalysis (0.93-1.12 days). For WTG approximation (not shown), the slope of $\langle Q_1 \rangle'$ versus $\langle \omega \partial_p s \rangle'$ in reanalysis is 0.99. The values of the 25 models range from 0.98 to 1.06, and the multi-model mean is 1.01±0.02. The correlation between $\langle Q_1 \rangle'$ and $\langle \omega \partial_p s \rangle'$ is higher than 0.99 in the ERA5 and all models included. It suggests that these simulations largely satisfy the WTG balance over the IO region, so this criterion is not shown in Figure 1. $S_{q,m}$ in ERA5 is approximately 0.98 (Fig. 1). The mean of the 25 models is $\sim 0.92 \pm 0.06$, with most models showing values ranging from 0.89 to 1.02 (within 1.5 SD relative to ERA5). However, the $S_{q,m}$ in the 11 models are lower than 0.9, particularly for the IITM-ESM and MPI-ESM-1-2-HAM models (< 0.85). The relatively low $S_{q,m}$ values indicate that the contribution of $\langle s \rangle'$ to $\langle m \rangle'$ is more significant. All models and reanalysis have a high correlation coefficient (> 0.98) between moisture and MSE anomalies (not shown).

The $log_{10}\mathrm{N}_{mode}$ value of ERA5 is approximately -0.69 ($\mathrm{N}_{mode} \sim 0.2$), indicating that MJO exhibits moisture mode behavior over the IO region, in agreement with Mayta and Adames Corraliza (2023). Eight models depict a $log_{10}\mathrm{N}_{mode} > -0.3$ ($\mathrm{N}_{mode} > 0.5$), implying that their wave behavior is far from the moisture mode regime. It is worth noting that some models show almost good results for the first three moisture mode criteria but have $log_{10}\mathrm{N}_{mode} > -0.25$ (e.g., ACCESS-CM2, HadGEM3-GC31-MM, and KACE-1-0-G). Á. F. Adames et al. (2019) and Á. F. Adames (2022) performed a scale analysis and demonstrated that N_{mode} is largely determined by the phase speed of the wave. These models, as expected, simulate a faster MJO phase speed ($c_p > 8\ ms^{-1}$) than ERA5 (Fig. S1). A high sensitivity of N_{mode} to c_p was found in these 25 CMIP6 models (further discussion in SI). On the other hand, the $log_{10}\mathrm{N}_{mode} < -0.8$ ($\mathrm{N}_{mode} < 0.16$; e.g., AWI-ESM-1-1-LR, IITM-ESM, IPSL-CM6A-LR-INCA, MPI-ESM-1-2-HAM, MPI-ESM1-2-HR, and MPI-ESM1-2-LR) are models with near stationary MJO-like behavior ($c_p < 2.2\ ms^{-1}$).

According to the moisture mode criteria for the MJO's behavior (e.g., $R_{P,q}$ >0.9, $\tau_c \sim 1$ day, $S_{q,m} \sim 1$, and that $log_{10}\mathrm{N}_{mode}$ ranges within -0.8 to -0.5; marked by the blue values in Fig. 1), no model accurately captures all the MJO's moisture mode properties as previously observed. However, some models still have reasonable values close to the observations but with a slightly long τ_c or low $S_{q,m}$.

4 Comparison between observations, Good and Poor Models

In this section, we further discuss whether these models have better skills associated with the MJO simulation than others if they can approximately capture the moisture mode behavior. To this end, we consider the relaxed criteria ranges within ± 1.5 SD relative to the reanalysis for $R_{P,q}$, τ_c, and $S_{q,m}$ (green boxes in Fig. 1). $R_{P,q}$ and τ_c must be considered as one criterion. $log_{10}\mathrm{N}_{mode}$ should be -0.8 to -0.3 (orange boxes) because $log_{10}\mathrm{N}_{mode} < -0.3$ represents a higher contribution from the moisture fluctuation than the temperature fluctuation ($\mathrm{N}_{mode} < 0.5$). Based on these conditions, four relatively good models (RGMs; CESM2-FV2, EC-Earth3, GFDL-CM4, and MIROC6) and four relatively poor models (RPMs; AWI-ESM-1-1-LR, INM-CM4-8, IPSL-CM6A-LR-INCA, and MPI-ESM-1-2-HAM) are selected. We do not adopt more than one model from the same research institution to avoid the multi-model means that are dominated by similar simulations. If the models are from the same research center, the model with the best (worst) performance was selected in the relatively good (poor) model groups. For instance, in the poor model group, we selected MPI-ESM-1-2-HAM rather than MPI-ESM1-2-LR because the former has a lower values in τ_c and $S_{q,m}$ than the latter.

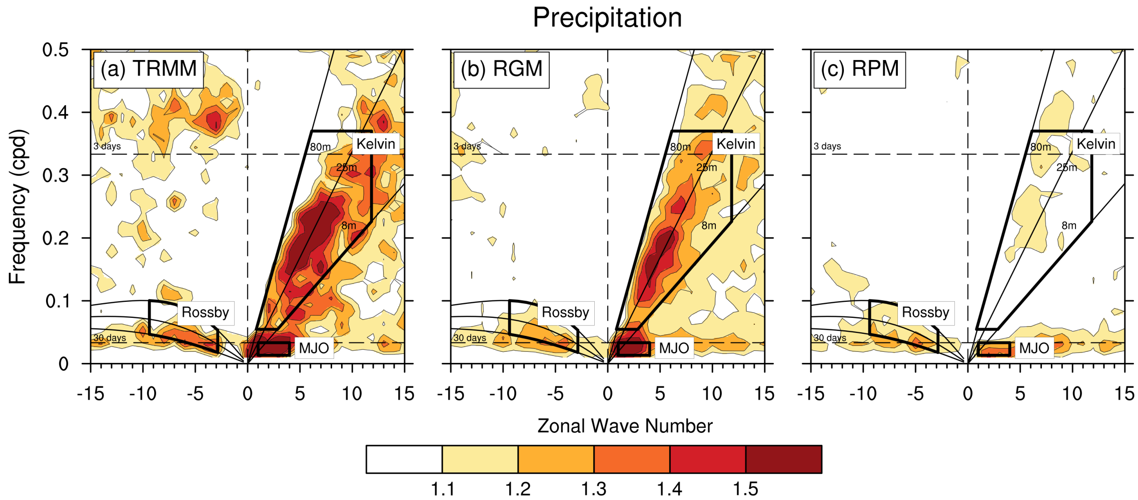

Figure 2. Space-time spectrum of the precipitation averaged between 10°S and 10°N for (a) TRMM, (b) the RGMs ensemble , and (c) the RPMs ensemble. The solid dispersion curves correspond to 8 m, 25 m, and 80 m equivalent depths. Color shading interval is 0.1.

4.1 Space-Time Spectrum

First, we computed space-time power spectra, making use of the fast Fourier transform (FFT). The calculation procedure is similar to those used by previous studies (e.g., Wheeler & Kiladis, 1999; Rushley et al., 2019; Y. Li et al., 2022, among others). We used precipitation from TRMM, RGMs, and RPMs as an input for the calculation. The results of TRMM and ERA5 are similar (not shown), although the ERA5 reanalysis (1995-2014) has a longer period than TRMM observation (1998-2014).

Figure 2 shows the symmetric power spectra of precipitation in the frequency-wavenumber domain. For the MJO band (wavenumber $k = 1 - 4$, and period of $30 - 90$ days), the TRMM and ensemble good models show strong spectra (power > 1.5), whereas it is relatively weak in the poor model group (power < 1.4). While precipitation exhibits a strong Kelvin wave signal in the observation and RGMs, such a signal is largely weak in the RPMs. Overall, the good model group can capture better wave signals and intensities than the poor model group.

4.2 Mean State

In previous studies, advection of the mean MSE has been found to be critical for MJO simulation (e.g., Jiang, 2017; Ahn et al., 2020; Ren et al., 2021, and others). On the other hand, the absence of mean low-level westerly winds in the western Pacific can lead to a non-propagating MJO in the model simulation (Inness & Slingo, 2003). Thus, it is worthwhile to compare the mean-state column-integrated MSE and 850-hPa zonal winds between the reanalysis, RGM, and RPM (Fig. 3). The pattern correlation (Cor) and root mean square deviation (RMSD) between the individual model group and the reanalysis are also shown in the upper right corner of each panel in Figure 3.

For ERA5, the relatively high column MSE is concentrated over the Indo-Pacific warm pool and decreases with higher latitude (Fig. 3a). The models simulate a similar but underestimated column MSE distribution compared with the reanalysis. The RGM has a higher column MSE over the equatorial warm pool relative to the RPM, especially in the western Pacific with the MSE extreme. This leads to stronger background zonal

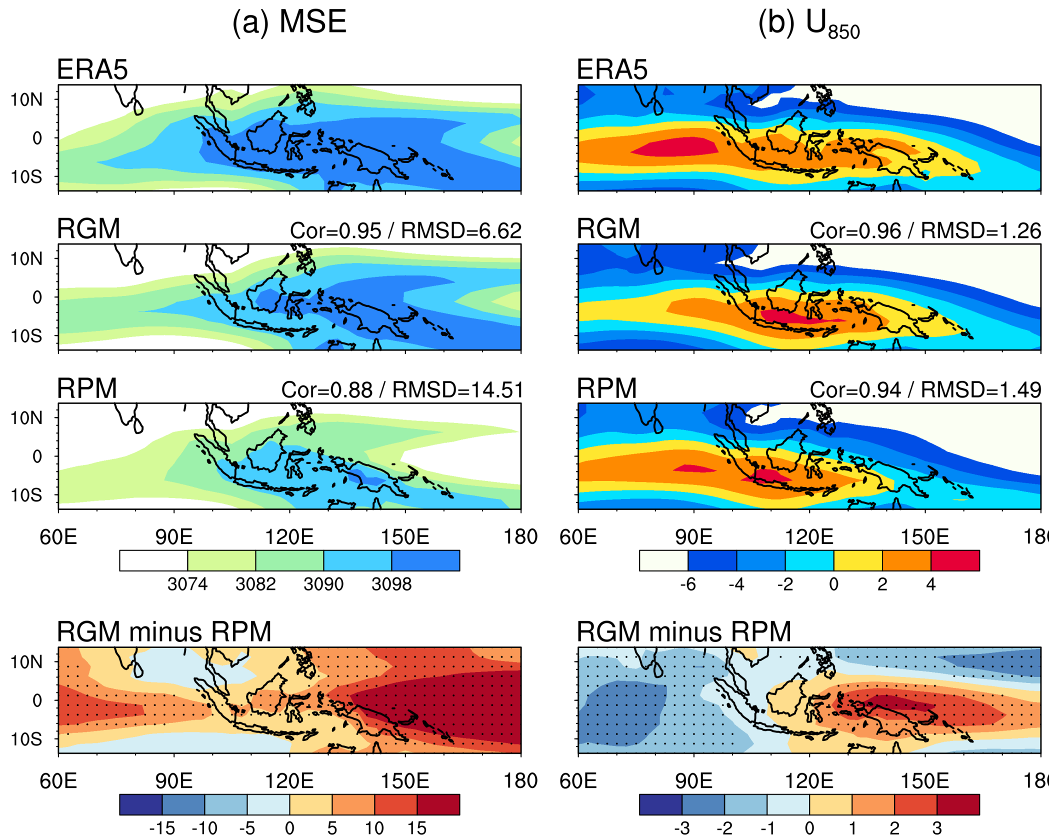

Figure 3. Spatial pattern of mean-state (a) column-integrated MSE (10^6 Jm^{-2}) and (b) 850-hPa zonal wind (ms^{-1}) for the boreal winter, derived from (top) the ERA5, (middle top) ensemble good model, (middle bottom) ensemble poor model group, and (bottom) the difference between RGM and RPM (RGM minus RPM). The gray dots in the bottom panels indicate statistical significance at the 95% confidence level. The pattern correlation (Cor) / root-mean-square deviation (RMSD) between the model group and reanalysis is presented at the top-right corners, respectively.

and meridional gradients of MSE in the good model group than in the poor model group. The observed westerlies cover the tropical warm pool from 60°E to 165°E, while the maximum wind speed occurs in the IO region (Fig. 3b). For the model simulation, the peak of zonal winds appears near the Maritime Continent, resulting in weaker westerlies over the IO region than reanalysis. In addition, the good model group simulates weaker (stronger) westerlies than the poor model group in the Indian Ocean (western Pacific) region. The westerlies can extend toward 160°E in the RGM; however, they are replaced by the strong easterly winds at 140°E in the RPM, especially for AWI-ESM-1-1-LR, INM-CM4-8 and IPSL-CM6A-LR-INCA (not shown), where the absence of background westerlies might partially explains why their MJO convection can not propagate across the Maritime Continent (Fig. S1).

4.3 Moist Static Energy Budget Analysis

The MSE budget is widely used to investigate the moist energy recharging and discharging associated with the MJO evolution (Inoue & Back, 2015; Ren et al., 2021; W.-L. Tseng et al., 2022, and others), taking the following form:

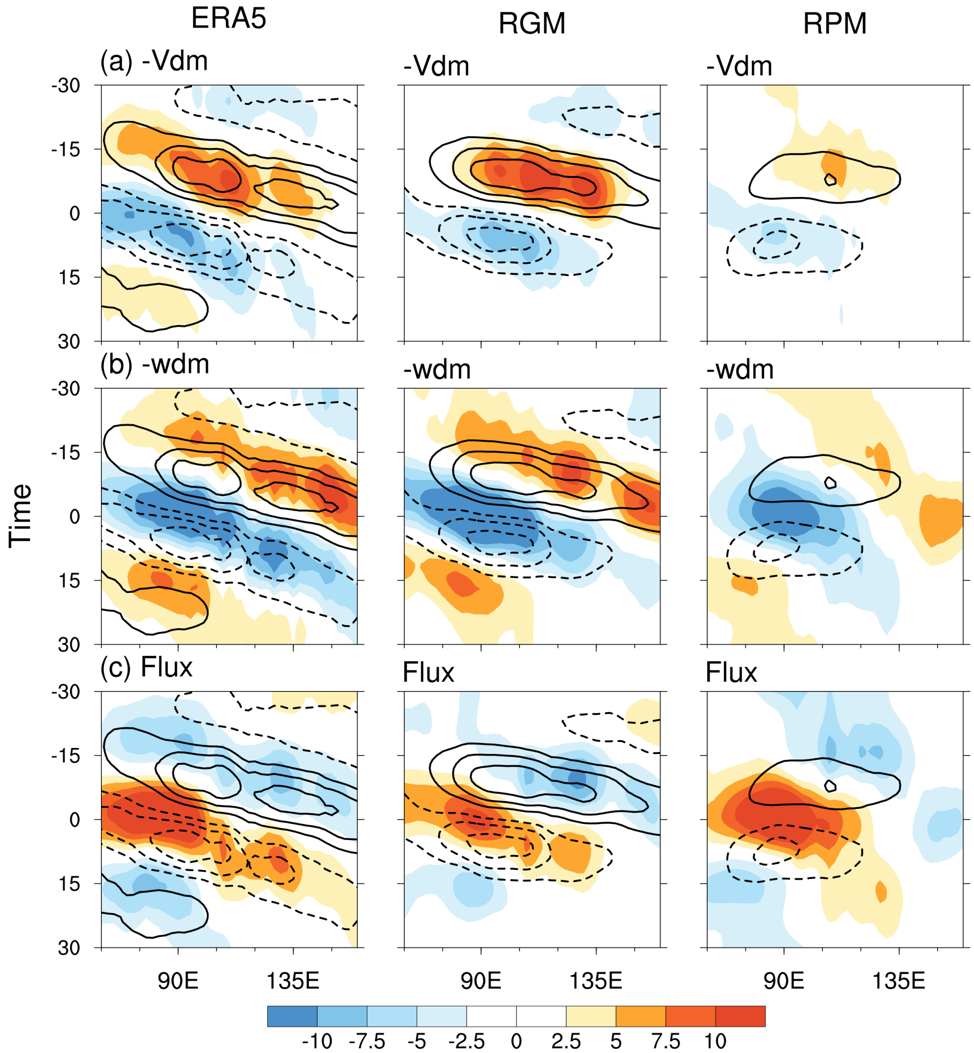

Figure 4. Hovmöller diagram of regressed MSE budget terms (shading) and $\langle \partial_t m \rangle'$ (contour) averaged between 10°S and 10°N from -30 to 30 days for the ERA5 (left panel), RGM (middle panel) and RPM (right panel). The individual terms are (a) $\langle -\mathbf{v} \cdot \nabla m \rangle'$, (b) $\langle -\omega \partial_p m \rangle'$, and (c) $Flux'$. The contour and shading intervals are 2 and 2.5 W m^{-2}, respectively.

$$\langle \partial_t m \rangle' = \langle -\mathbf{v} \cdot \nabla m \rangle' + \langle -\omega \partial_p m \rangle' + Flux' \tag{5}$$

where the left-side term in Eq. (5) is the MSE tendency. The first and second terms on the right-side represent the horizontal and vertical MSE advection, respectively. The other term of Eq. (5) is the flux term ($Flux' = \langle Q_r \rangle' + L_v E' + SH'$) that includes the column radiative flux $\langle Q_r \rangle'$, surface latent heat flux $L_v E'$, and surface sensible heat flux SH'.

Figure 4 shows the Hovmöller diagram of the regressed MSE budget terms in Eq. 5 for the ERA5 and model groups. The MSE budget terms display an eastward propagation in the reanalysis (Fig. 4a). $\langle -\mathbf{v} \cdot \nabla m \rangle'$ varies in phase with $\langle \partial_t m \rangle'$. RGM simulations reproduce the eastward MJO convection with strong $\langle -\mathbf{v} \cdot \nabla m \rangle'$ and $\langle \partial_t m \rangle'$. The RPM exhibits weak and nearly non-propagating convection. In Figure 4b, $\langle -\omega \partial_p m \rangle'$

leads $\langle \partial_t m \rangle'$ in the reanalysis and the models. Compared with ERA5, $\langle -\omega \partial_p m \rangle'$ has a stronger drying effect (< 0) in the RGM and an underestimated amplitude in the RPM. The observed $Flux'$ exhibits a lagged evolution with $\langle \partial_t m \rangle'$ (Fig. 4c). The simulated $Flux'$ of RGM is weaker than the reanalysis, whereas the positive $Flux'$ in the RPM can not propagate into the western Pacific.

5 Summary and Conclusions

In this study, we applied the moisture mode theory-based diagnosis (Ahmed et al., 2021; Mayta et al., 2022; Mayta & Adames Corraliza, 2023) to assess the moisture mode properties of MJO over the Indian Ocean (10°S-10°N, 75E°-100°E) in the 25 CMIP6 models. The following are answers to the two questions based on the results in Sections 3 to 4:

Q1: Can the global climate models reproduce the MJO moisture mode properties over the Indian Ocean?

Our results demonstrate that none of the models used in this study could reliably reproduce all moist thermodynamic properties of the MJO as observed in Figure 1: (i) Few models showed a high correlation (greater than 0.9) between moisture and precipitation anomalies and exhibited convective adjustment time scale (τ_c) that aligned with the reanalysis; (ii) All models can satisfy the criteria for weak temperature gradient (WTG) balance; (iii) Nevertheless, 11 models still exhibited an unrealistically high contribution from temperature fluctuations to the MSE anomalies; and (iv) limited number of models showed values of N_{mode} that are close to those of the reanalysis data. High values of N_{mode} ($\gg 0.5$) or low N_{mode} ($\ll 0.16$) imply that many models showed unrealistically fast or nearly non-propagating MJO convection, respectively.

Q2: If a model can capture the moisture mode behaviors, does it mean that the model has better skills in the MJO simulation than others?

While no model fully captures the behavior of the MJO, there is a subset that performs reasonably well. These good models (e.g., CESM2-FV2, EC-Earth3, GFDL-CM4, and MIROC6) were selected based on their acceptable performance in the moisture mode criteria (Fig. 1). They also show a stronger wave response of the MJO signals compared to the relatively poor models (Fig. 2). The good model group realistically simulates the mean-state column MSE and low-level zonal winds (Fig. 3). MSE budget associated with the MJO is better represented in the good models rather than in the poor models group, especially in the MSE advection terms (Fig. 4). Our results indicate that models accurately capturing the moisture mode behavior of the MJO over the Indian Ocean demonstrate improved simulation of the MJO.

Most of these "acceptable" good models also depicted good performance in the MJO metrics proposed by previous studies (Ahn et al., 2020; Orbe et al., 2020; G. Chen et al., 2022; Y. Li et al., 2022). A robust MJO propagation is correlated with a more humid mean state with stronger horizontal moisture gradients, as well as more robust MJO wind anomalies (Ahn et al., 2020; Y. Li et al., 2022). This consistency makes sense since many previous studies have obtained these results under the a-priori assumption that the MJO behaves as a moisture mode. In other words, many previous studies implicitly assume that the moisture mode criteria are always satisfied, and that good MJO models are those that best simulate the processes that lead to the destabilization and propagation of moisture modes. These include having stronger horizontal moisture gradients that lead to more robust propagation via horizontal moisture advection, convection that is more sensitive to moisture variations, and a small effective gross moist stability (e.g., Benedict et al., 2014; Ahn et al., 2017, 2020).

Our study extends upon previous by showing that the expected moisture mode behavior only exists in models that more robustly simulate the MJO. Thus, the relatively good MJO models do not just simulate the processes that lead to the destabilization and propagation of moisture modes, they are also the models that best simulate the moisture mode behavior of the MJO over the Indian Ocean. Poorer models not only have weaker or non-propagating MJO-like variability, but this variability is inconsistent with moisture mode behavior. Thus, simulating an MJO that behaves as a moisture mode over the Indian may be synonymous with simulating a realistic MJO, and the four criteria used here appear to be useful diagnostic tools for evaluating MJO simulation performance.

In spite of these findings, we cannot say whether simulating the moisture mode behavior is what causes the models to perform better. It may be related to more realistic convection representation, or a combination of other factors. More work is needed to better understand the causality.

6 Open Research

We downloaded the CMIP6 model simulation outputs from the Lawrence Livermore National Laboratory (`https://esgf-node.llnl.gov/search/cmip6`). The interpolated OLR data was obtained from the NOAA (`https://psl.noaa.gov/data/gridded/data.interp_OLR.html`). The precipitation from Tropical Rainfall Measuring Mission (3B42) dataset was downloaded from the NASA (`https://disc.gsfc.nasa.gov/`). The reanalysis data was available at ECMWF (ERA5; `https://doi.org/10.24381/cds.adbb2d47`).

Acknowledgments

QJL was sponsored by the Ministry of Science and Technology (MOST) of Taiwan under Grants MOST111-2917-I-008-002 and NSF CAREER grant number 2236433. VM and ÁFAC were also supported by NOAA grant number NA22OAR4310611 and NSF CAREER grant number 2236433.

References

Adames, Á. F. (2017). Precipitation budget of the Madden–Julian oscillation. *Journal of the Atmospheric Sciences*, *74*(6), 1799–1817.

Adames, Á. F. (2022). The Basic Equations UnderWeak Temperature Gradient Balance: Formulation, Scaling, and Types of Convectively-coupled Motions. *Journal of the Atmospheric Sciences*.

Adames, Á. F., & Kim, D. (2016). The MJO as a dispersive, convectively coupled moisture wave: Theory and observations. *Journal of the Atmospheric Sciences*, *73*(3), 913–941.

Adames, Á. F., Kim, D., Clark, S. K., Ming, Y., & Inoue, K. (2019). Scale analysis of moist thermodynamics in a simple model and the relationship between moisture modes and gravity waves. *Journal of the Atmospheric Sciences*, *76*(12), 3863–3881.

Adames, A. F., & Maloney, E. D. (2021). Moisture mode theory's contribution to advances in our understanding of the Madden-Julian oscillation and other tropical disturbances. *Current Climate Change Reports*, *7*, 72–85.

Adames, Á. F., Powell, S. W., Ahmed, F., Mayta, V. C., & Neelin, J. D. (2021). Tropical precipitation evolution in a buoyancy-budget framework. *Journal of the Atmospheric Sciences*, *78*(2), 509–528.

Adames, Á. F., & Wallace, J. M. (2015). Three-dimensional structure and evolution of the moisture field in the MJO. *Journal of the Atmospheric Sciences*, *72*(10), 3733–3754.

Ahmed, F., Neelin, J. D., & Adames, Á. F. (2021). Quasi-equilibrium and weak temperature gradient balances in an equatorial beta-plane model. *Journal of the Atmospheric Sciences*, *78*(1), 209–227.

Ahn, M.-S., Kim, D., Kang, D., Lee, J., Sperber, K. R., Gleckler, P. J., … Kim, H. (2020). MJO propagation across the Maritime Continent: Are CMIP6 models better than CMIP5 models? *Geophysical Research Letters*, *47*(11), e2020GL087250.

Ahn, M.-S., Kim, D., Sperber, K. R., Kang, I.-S., Maloney, E., Waliser, D., & Hendon, H. (2017). MJO simulation in CMIP5 climate models: MJO skill metrics and process-oriented diagnosis. *Climate Dynamics*, *49*(11), 4023–4045.

Bagtasa, G. (2020). Influence of Madden–Julian oscillation on the intraseasonal variability of summer and winter monsoon rainfall in the Philippines. *Journal of Climate*, *33*(22), 9581–9594.

Benedict, J. J., Maloney, E. D., Sobel, A. H., & Frierson, D. M. (2014). Gross moist stability and mjo simulation skill in three full-physics gcms. *Journal of the Atmospheric Sciences*, *71*(9), 3327–3349.

Betts, A. K. (1986). A new convective adjustment scheme. Part I: Observational and theoretical basis. *Quarterly Journal of the Royal Meteorological Society*, *112*(473), 677–691.

Chang, C.-H., Johnson, N. C., & Yoo, C. (2021). Evaluation of subseasonal impacts of the MJO/BSISO in the East Asian extended summer. *Climate Dynamics*, *56*(11), 3553-3568.

Chen, G., Ling, J., Zhang, R., Xiao, Z., & Li, C. (2022). The MJO from CMIP5 to CMIP6: Perspectives from tracking MJO precipitation. *Geophysical Research Letters*, *49*(1), e2021GL095241.

Chen, J.-M., Wu, C.-H., Chung, P.-H., & Sui, C.-H. (2018). Influence of intraseasonal–interannual oscillations on tropical cyclone genesis in the western North Pacific. *Journal of Climate*, *31*(12), 4949-4961.

Cowan, T., Wheeler, M. C., & Marshall, A. G. (2022). The combined influence of the Madden-Julian Oscillation and El Niño-Southern Oscillation on Australian rainfall. *Journal of Climate*, 1–44.

Dao, T. L., Vincent, C. L., & Lane, T. P. (2023). Multiscale influences on rainfall in northeast australia. *Journal of Climate*, *36*(17), 5989–6006.

Del Genio, A. D., & Chen, Y. (2015). Cloud-radiative driving of the Madden-Julian oscillation as seen by the A-Train. *Journal of Geophysical Research: Atmospheres*, *120*(11), 5344–5356.

Emanuel, K. A., David Neelin, J., & Bretherton, C. S. (1994). On large-scale circulations in convecting atmospheres. *Quarterly Journal of the Royal Meteorological Society*, *120*(519), 1111–1143.

Eyring, V., Bony, S., Meehl, G. A., Senior, C. A., Stevens, B., Stouffer, R. J., & Taylor, K. E. (2016). Overview of the Coupled Model Intercomparison Project Phase 6 (CMIP6) experimental design and organization. *Geoscientific Model Development*, *9*(5), 1937–1958.

Hendon, H. H., Wheeler, M. C., & Zhang, C. (2007). Seasonal dependence of the MJO–ENSO relationship. *Journal of climate*, *20*(3), 531–543.

Hersbach, H., Bell, B., Berrisford, P., Horányi, A., Sabater, J. M., Nicolas, J., … others (2019). Global reanalysis: goodbye era-interim, hello era5. *ECMWF newsletter*, *159*, 17–24.

Holloway, C. E., Woolnough, S. J., & Lister, G. M. (2013). The effects of explicit versus parameterized convection on the MJO in a large-domain high-resolution tropical case study. Part I: Characterization of large-scale organization and propagation. *Journal of the Atmospheric Sciences*, *70*(5), 1342–1369.

Hung, C.-S., & Sui, C.-H. (2018). A diagnostic study of the evolution of the MJO from Indian Ocean to Maritime Continent: Wave dynamics versus advective moistening processes. *Journal of Climate*, *31*(10), 4095–4115.

Inness, P. M., & Slingo, J. M. (2003). Simulation of the madden–julian oscillation in a coupled general circulation model. part i: Comparison with observations and an atmosphere-only gcm. *Journal of Climate*, *16*(3), 345–364.

Inoue, K., & Back, L. (2015). Column-integrated moist static energy budget analysis on various time scales during toga coare. *Journal of the Atmospheric Sciences*, *72*(5), 1856–1871.

Jiang, X. (2017). Key processes for the eastward propagation of the madden-julian oscillation based on multimodel simulations. *Journal of Geophysical Research: Atmospheres*, *122*(2), 755–770.

Kim, D., Kug, J.-S., & Sobel, A. H. (2014). Propagating versus nonpropagating Madden–Julian oscillation events. *Journal of Climate*, *27*(1), 111–125.

Kim, D., Lee, M.-I., Kim, D., Schubert, S. D., Waliser, D. E., & Tian, B. (2014). Representation of tropical subseasonal variability of precipitation in global reanalyses. *Climate dynamics*, *43*, 517–534.

Kim, D., Sperber, K., Stern, W., Waliser, D., Kang, I.-S., Maloney, E., … others (2009). Application of mjo simulation diagnostics to climate models. *Journal of Climate*, *22*(23), 6413–6436.

Kiranmayi, L., & Maloney, E. D. (2011). Intraseasonal moist static energy budget in reanalysis data. *Journal of Geophysical Research: Atmospheres*, *116*(D21).

Kummerow, C., Simpson, J., Thiele, O., Barnes, W., Chang, A., Stocker, E., … others (2000). The status of the Tropical Rainfall Measuring Mission (TRMM) after two years in orbit. *Journal of applied meteorology*, *39*(12), 1965–1982.

Lee, J., Sperber, K. R., Gleckler, P. J., Bonfils, C. J., & Taylor, K. E. (2019). Quantifying the agreement between observed and simulated extratropical modes of interannual variability. *Climate Dynamics*, *52*(7), 4057–4089.

Lee, M.-I., Kang, I.-S., & Mapes, B. E. (2003). Impacts of cumulus convection parameterization on aqua-planet AGCM simulations of tropical intraseasonal variability. *Journal of the Meteorological Society of Japan. Ser. II*, *81*(5), 963–992.

Lee, S.-K., Lopez, H., Tuchen, F. P., Kim, D., Foltz, G. R., & Wittenberg, A. T. (2023). On the genesis of the 2021 Atlantic Niño. *Geophysical Research Letters*, *50*(16), e2023GL104452.

Lee, Y.-Y., & Grotjahn, R. (2019). Evidence of specific MJO phase occurrence with summertime California Central Valley extreme hot weather. *Advances in Atmospheric Sciences*, *36*(6), 589-602.

Li, X., Yin, M., Chen, X., Yang, M., Xia, F., Li, L., … Zhang, C. (2020). Impacts of the Tropical Pacific–Indian Ocean Associated Mode on Madden–Julian Oscillation over the Maritime Continent in Boreal Winter. *Atmosphere*, *11*(10), 1049.

Li, Y., Wu, J., Luo, J.-J., & Yang, Y. M. (2022). Evaluating the Eastward Propagation of the MJO in CMIP5 and CMIP6 Models Based on a Variety of Diagnostics. *Journal of Climate*, *35*(6), 1719–1743.

Liebmann, B., & Smith, C. A. (1996). Description of a complete (interpolated) outgoing longwave radiation dataset. *Bulletin of the American Meteorological Society*, *77*(6), 1275–1277.

Madden, R. A., & Julian, P. R. (1971). Detection of a 40–50 Day Oscillation in the Zonal Wind in the Tropical Pacific. *Journal of Atmospheric Sciences*, *28*(5), 702-708.

Madden, R. A., & Julian, P. R. (1972). Description of Global-Scale Circulation Cells in the Tropics with a 40–50 Day Period. *Journal of Atmospheric Sciences*, *29*(6), 1109-1123.

Maloney, E. D., & Hartmann, D. L. (2001). The sensitivity of intraseasonal variability in the NCAR CCM3 to changes in convective parameterization. *Journal of Climate*, *14*(9), 2015–2034.

Maloney, E. D., Sobel, A. H., & Hannah, W. M. (2010). Intraseasonal variability in an aquaplanet general circulation model. *Journal of Advances in Modeling Earth Systems*, *2*(2).

Mayta, V. C., & Adames, Á. F. (2023). Moist thermodynamics of convectively coupled waves over the western hemisphere. *Journal of Climate*, 1–35.

Mayta, V. C., Adames, Á. F., & Ahmed, F. (2022). Westward-Propagating Moisture Mode Over the Tropical Western Hemisphere. *Geophysical Research Letters*, *49*(6), e2022GL097799.

Mayta, V. C., & Adames Corraliza, Á. F. (2023). Is the Madden-Julian Oscillation a Moisture Mode? *Geophysical Research Letters*, *50*(15), e2023GL103002.

Mayta, V. C., Adames Corraliza, Á. F., & Lin, Q.-J. (2023). The radon and hilbert transforms and their applications to atmospheric waves. *Atmospheric Science Letters*, *In Revision*(n/a).

Mayta, V. C., Kiladis, G. N., Dias, J., Silva Dias, P. L., & Gehne, M. (2021). Convectively coupled Kelvin waves over tropical South America. *Journal of Climate*, *34*(16), 6531–6547.

Miller, D. E., Gensini, V. A., & Barrett, B. S. (2022). Madden-Julian oscillation influences United States springtime tornado and hail frequency. *npj Climate and Atmospheric Science*, *5*(1), 1–8.

Orbe, C., Van Roekel, L., Adames, Á. F., Dezfuli, A., Fasullo, J., Gleckler, P. J., … others (2020). Representation of modes of variability in six US climate models. *Journal of Climate*, *33*(17), 7591–7617.

Radon, J. (1917). Uber die bestimmung von funktionen durch ihre intergralwerte la'ngs gewisser mannigfaltikeiten. *Ber. Sa'chsische Akad. Wiss*, 69–262.

Rahul, R., Kuttippurath, J., Chakraborty, A., & Akhila, R. (2022). The inverse influence of MJO on the cyclogenesis in the north Indian Ocean. *Atmospheric Research*, *265*, 105880.

Raymond, D. J., & Fuchs, Ž. (2009). Moisture modes and the Madden–Julian oscillation. *Journal of Climate*, *22*(11), 3031–3046.

Ren, P., Kim, D., Ahn, M.-S., Kang, D., & Ren, H.-L. (2021). Intercomparison of MJO column moist static energy and water vapor budget among six modern reanalysis products. *Journal of Climate*, *34*(8), 2977–3001.

Rushley, S. S., Janiga, M. A., Ridout, J. A., & Reynolds, C. A. (2022). The Impact of Mean State Moisture Biases on MJO Skill in the Navy ESPC. *Monthly Weather Review*.

Rushley, S. S., Kim, D., & Adames, Á. F. (2019). Changes in the MJO under greenhouse gas–induced warming in CMIP5 models. *Journal of Climate*, *32*(3), 803–821.

Sobel, A., & Maloney, E. (2012). An idealized semi-empirical framework for modeling the madden–julian oscillation. *Journal of the Atmospheric Sciences*, *69*(5), 1691–1705.

Sobel, A., & Maloney, E. (2013). Moisture modes and the eastward propagation of the MJO. *Journal of the Atmospheric Sciences*, *70*(1), 187–192.

Sobel, A., Wang, S., & Kim, D. (2014). Moist static energy budget of the mjo during dynamo. *Journal of the Atmospheric Sciences*, *71*(11), 4276–4291.

Tseng, K.-C., Sui, C.-H., & Li, T. (2015). Moistening processes for madden–julian oscillations during dynamo/cindy. *Journal of Climate*, *28*(8), 3041–3057.

Tseng, W.-L., Hsu, H.-H., Lan, Y.-Y., Lee, W.-L., Tu, C.-Y., Kuo, P.-H., … Liang, H.-C. (2022). Improving Madden–Julian oscillation simulation in atmospheric general circulation models by coupling with a one-dimensional snow–ice–thermocline ocean model. *Geoscientific Model Development*, *15*(14), 5529–5546.

Wang, B., Liu, F., & Chen, G. (2016). A trio-interaction theory for Madden–Julian oscillation. *Geoscience Letters*, *3*(1), 1–16.

Wheeler, M., & Kiladis, G. N. (1999). Convectively coupled equatorial waves: Analysis of clouds and temperature in the wavenumber–frequency domain. *Journal*

of the Atmospheric Sciences, *56*(3), 374–399.
Zhang, B., Kramer, R. J., & Soden, B. J. (2019). Radiative feedbacks associated with the Madden–Julian oscillation. *Journal of Climate*, *32*(20), 7055–7065.
Zhang, C., & Ling, J. (2017). Barrier effect of the Indo-Pacific Maritime Continent on the MJO: Perspectives from tracking MJO precipitation. *Journal of Climate*, *30*(9), 3439–3459.
Zhang, Q., Li, T., & Liu, J. (2019). Contrast of evolution characteristics of boreal summer and winter intraseasonal oscillations over tropical Indian Ocean. *Journal of Meteorological Research*, *33*(4), 678–694.

Figure 1.

	$R_{P,q}$	τ_c	$S_{q,m}$	$\log_{10} N_{mode}$	
ERA5	0.95	1.02	0.98	-0.69	
ACCESS-CM2	0.88	1.10	0.96	-0.06	
AWI-ESM-1-1-LR	0.92	0.86	0.86	-0.97	✕
BCC-ESM1	0.86	0.83	0.89	-0.64	
CESM2	0.85	1.15	0.87	-0.60	
CESM2-FV2	0.92	1.11	0.89	-0.61	○
CESM2-WACCM	0.86	1.05	0.92	-0.57	
CESM2-WACCM-FV2	0.88	1.15	0.89	-0.39	
EC-Earth3	0.89	1.28	1.00	-0.65	○
FGOALS-g3	0.87	1.08	0.87	-0.69	
GFDL-CM4	0.90	0.93	0.90	-0.45	○
HadGEM3-GC31-LL	0.94	1.19	0.97	-0.25	
HadGEM3-GC31-MM	0.92	1.15	0.94	-0.05	
IITM-ESM	0.93	0.99	0.82	-0.98	
INM-CM4-8	0.76	1.08	1.02	-0.02	✕
INM-CM5-0	0.80	0.95	1.01	0.00	
IPSL-CM6A-LR	0.84	1.10	0.95	-0.68	
IPSL-CM6A-LR-INCA	0.79	0.98	0.88	-1.03	✕
KACE-1-0-G	0.94	1.27	0.95	0.28	
MIROC6	0.88	1.20	0.92	-0.75	○
MPI-ESM-1-2-HAM	0.88	0.60	0.83	-0.94	✕
MPI-ESM1-2-HR	0.91	0.83	0.87	-0.94	
MPI-ESM1-2-LR	0.88	0.68	0.85	-0.94	
MRI-ESM2-0	0.88	1.30	1.00	-0.20	
TaiESM1	0.94	1.37	1.05	-0.49	
UKESM1-0-LL	0.92	1.27	0.94	-0.27	

Figure 2.


Precipitation
(a) TRMM
(b) RGM
(c) RPM
Frequency (cpd)
Zonal Wave Number
Kelvin
Rossby
MJO
3 days
30 days
80m
25m
8m
0.5
0.4
0.3
0.2
0.1
0
-15
-10
-5
0
5
10
15
1.1
1.2
1.3
1.4
1.5

Figure 3.

(a) MSE
(b) U850
ERA5
RGM
Cor=0.95 / RMSD=6.62
Cor=0.96 / RMSD=1.26
RPM
Cor=0.88 / RMSD=14.51
Cor=0.94 / RMSD=1.49
RGM minus RPM
10N
0
10S
60E
90E
120E
150E
180
3074
3082
3090
3098
-6
-4
-2
0
2
4
-15
-10
-5
0
5
10
15
-3
-2
-1
0
1
2
3

Figure 4.

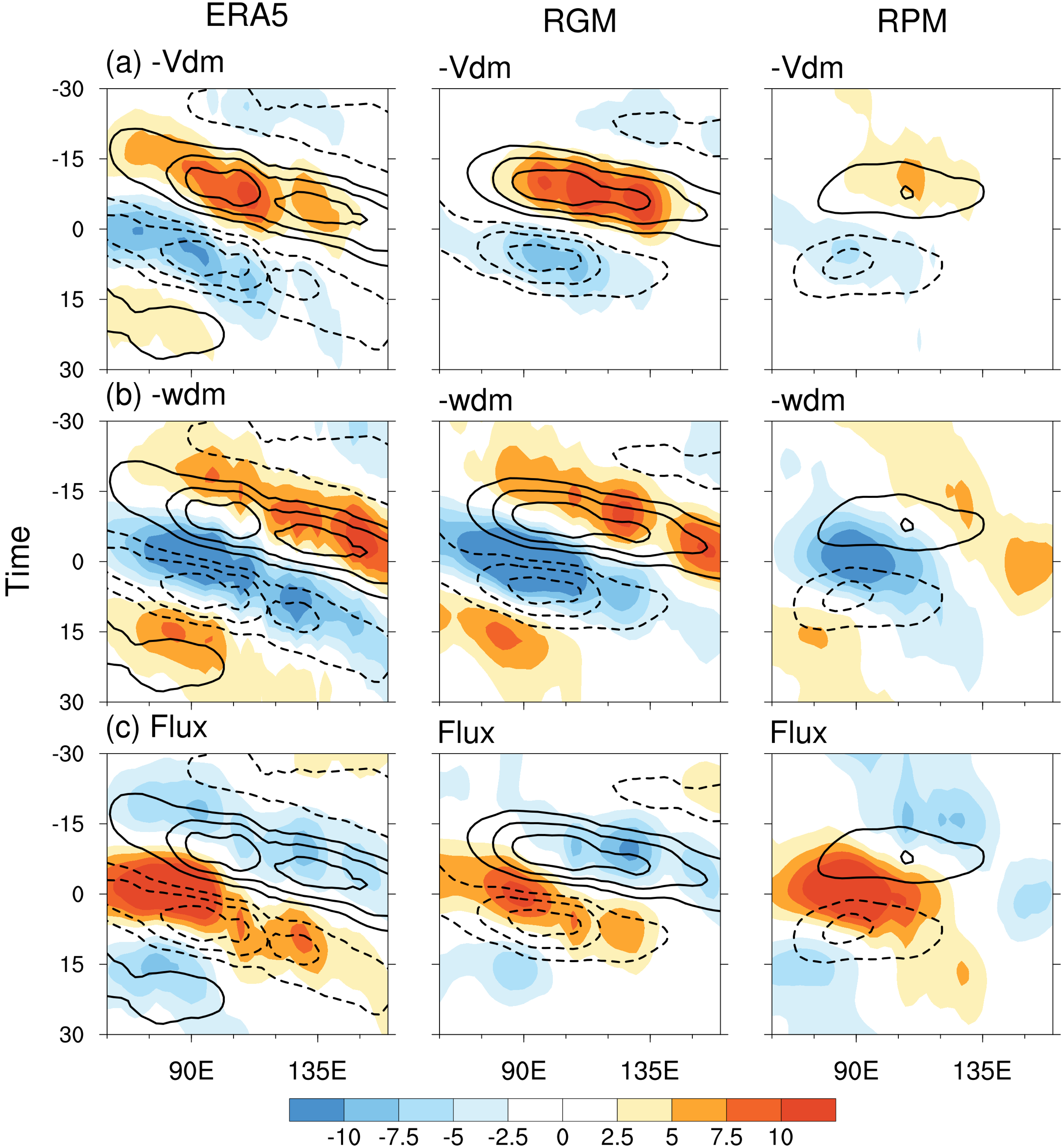

ERA5
RGM
RPM
(a) -Vdm
-Vdm
-Vdm
(b) -wdm
-wdm
-wdm
(c) Flux
Flux
Flux
Time
-30
-15
0
15
30
90E
135E
-10
-7.5
-5
-2.5
0
2.5
5
7.5
10